PHYSICAL REVIEW E **77**, 025601(R) (2008)

Far-field image magnification for acoustic waves using anisotropic acoustic metamaterials

Xianyu Ao* and C. T. Chan

Department of Physics, The Hong Kong University of Science and Technology, Clear Water Bay, Kowloon, Hong Kong, China

(Received 29 September 2007; published 6 February 2008)

A kind of two-dimensional acoustic metamaterial is designed so that it exhibits strong anisotropy along two orthogonal directions. Based on the rectangular equal frequency contour of this metamaterial, magnifying lenses for acoustic waves, analogous to electromagnetic hyperlenses demonstrated recently in the optical regime, can be realized. Such metamaterial may offer applications in imaging for systems that obey scalar wave equations.

DOI: 10.1103/PhysRevE.77.025601 PACS number(s): 43.20.+g, 43.35.+d, 43.40.+s

Subwavelength imaging in electromagnetic waves was first proposed by using a slab of left-handed medium (LHM) [1]. The propagating waves from a source are focused due to negative refraction [2] and the evanescent waves are amplified inside the slab by surface waves. Other kinds of mechanisms were also reported for subwavelength imaging [3,4]. In one mechanism called canalization [4,5], part of the equal-frequency surface is nearly flat and parallel to the slab interface, and the width of the flat part in k space is several times larger than the wave number of the background. Thus not only the propagating waves but also the evanescent waves from the source are converted into the propagating modes inside the slab, and transferred to the back interface to form a subwavelength image in the near field.

The image with subwavelength resolution by slablike superlenses mentioned above is in the near field. In some applications, a device capable of forming a magnified optical image in the far field of a subwavelength object is desired. It was proposed theoretically [6,7] and subsequently demonstrated experimentally in the optical region [8,9] that a curved version of anisotropic layered structures can transfer near-field subwavelength images to the far field and can magnify the features at the same time, so that an optical microscope in the far field can image the original subwavelength object (the so-called "hyperlens," as the system has a hyperbolic dispersion relation). The one-dimensional layered structures with alternate negative and positive permittivity provide the effective permittivity tensor with extreme anisotropy [10–15]. For a curved version of layered media, narrow beams from the source propagate along the radial direction via the canalization mechanism.

It would be of interest to generalize the concept of superlens and hyperlens to acoustic waves, and the realization may offer opportunities in application in areas such as ultrasonic imaging [16]. However, we see some immediate difficulty here. For electromagnetic waves, the permittivity and permeability can be negative, but natural material has neither a negative mass density nor a negative bulk modulus. Recent work on phononic crystals showed that negative refraction and focusing of acoustic waves can be obtained by Bragg scattering [17–19]. Substantial progress has also been made in the theoretical and experimental realization of acoustic metamaterials with (effective) negative modulus or negative density [20–26]. In this paper, we present a design of a type of acoustic metamaterial with strong anisotropy that can form a far-field image beyond the diffraction limit.

We start with a two-dimensional (2D) square array of coaxially layered rods in water. As shown in the inset of Fig. 1(a), the rod has three layers: inner steel core of radius $r_1=0.15a$, intermediate rubber coating of radius $r_2=0.20a$, and outer aluminum shell of radius $r_3=0.30a$, where a is the lattice constant. This is a kind of locally resonant acoustic

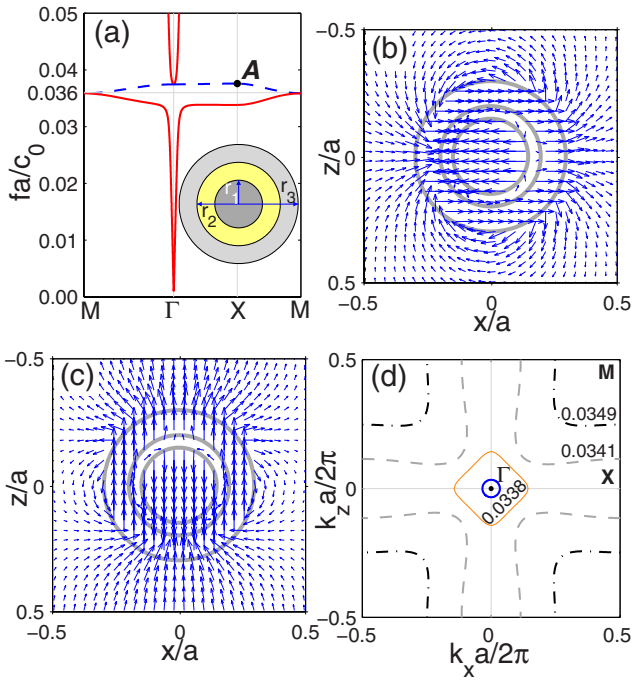

FIG. 1. (Color online) (a) Band structure for a square lattice. The dashed lines represent deaf bands (transverse modes). Inset is the schematic of the coaxially layered rod, with inner steel core of $r_1=0.15a$, rubber coating of $r_2=0.20a$, and outer aluminum shell of $r_3=0.30a$. (b) Displacement vector $\mathbf{u}=(u_x,u_z)$ for an acoustic plane wave (propagating along the x axis) incident on a single rod at the Mie resonance $fa/c_0=0.035\,865$. (c) Displacement vector $\mathbf{u}=(u_x,u_z)$ for the eigenmode labeled A in (a), with wave vector $\mathbf{k}$ parallel to the x axis. (d) Equal frequency contours in the first Brillouin zone for the frequencies near the lower edge of the resonant band gap. The numbers correspond to values of fa/c_0. The blue (dark gray) circle at the center is for the host at $fa/c_0=0.0338$.

*aoxy@ust.hk

metamaterial [20,27], which can exhibit a low-frequency resonant band gap. We note that the materials and the configuration parameters (such as the radii) used are chosen to illustrate the idea. We did not attempt an elaborate effort to optimize the parameters. By changing the dimension of the system and the materials being used, one can tune the working frequency and/or optimize the phenomenon for a particular working frequency. We use the following material parameters. A form of soft rubber [28] is assumed here with $\rho=1000\ \mathrm{kg/m^3}$, $c_l=55\ \mathrm{m/s}$, and $c_t=19\ \mathrm{m/s}$; for steel $\rho=7700\ \mathrm{kg/m^3}$, $c_l=5050\ \mathrm{m/s}$, and $c_t=3080\ \mathrm{m/s}$; for aluminum $\rho=2730\ \mathrm{kg/m^3}$, $c_l=6800\ \mathrm{m/s}$, and $c_t=3240\ \mathrm{m/s}$; and for water $\rho_0=1000\ \mathrm{kg/m^3}$ and $c_0=1490\ \mathrm{m/s}$. We consider the in-plane modes which are associated to motions in the plane perpendicular to the rod axis (assumed to be along the y axis). The elastic wave equation is solved by the multiple-scattering method [29–32].

Figure 1(a) shows the band structure of the square array, which indicates a low-frequency resonant band gap near $fa/c_0=0.036$. In order to clarify the character of the resonance, we show in Fig. 1(b) the displacement vector $\mathbf{u}=(u_x,u_z)$ for an acoustic plane wave (propagating along the x axis) incident on a single rod at its Mie resonance (at $fa/c_0=0.035\,865$, near the mid-gap frequency of the square array along Γ-X). We can see that the inner core and the outer shell move along the direction of propagation in opposite phase with respect to each other, via the linking of the intermediate rubber coating [27]. The conceptual model behind is basically a mass (the inner core) connected by a spring (the rubber) to a wall (the outer shell) [33], and the system vibrates with a dipolelike resonance. The dashed lines in Fig. 1(a) are transverse modes (deaf bands, as they do not couple with normal-incident longitudinal waves) corresponding to zero effective density. The eigenmode labeled A in Fig. 1(a) is shown in Fig. 1(c), and we can see that the wave vector and displacement vector are perpendicular to each other for this mode (so transverse).

The equal frequency contours (EFCs) for the frequencies near the lower edge of the resonant band gap are shown in Fig. 1(d). The EFC of $fa/c_0=0.0338$ is squarelike. Such a squarelike EFC implies collimation effect at this frequency along the Γ-M direction. A similar example was discussed in a two-dimensional electromagnetic crystal formed by a lattice of capacitively loaded wires [4]. For our case we find that this isotropic configuration is not appropriate for the far-field image magnification purpose, as will be discussed later.

To achieve anisotropy, we stretch the square lattice to a rectangular one, e.g., with lattice constants along x and z directions set as $a_x=a$ and $a_z=2a$ [see the inset of Fig. 2(a)]. Figure 2(a) shows the band structure of this rectangular array. The frequency range of the resonant gap along the Γ-X_1 direction (with $a_x=a$) is $0.035\,66<fa/c_0<0.037\,52$, and that for Γ-X_2 (with $a_z=2a$) is $0.033\,85<fa/c_0<0.035\,80$. By comparing with Fig. 1(a), we see that the lower edge of the resonant gap along the Γ-X_1 direction moves up, and the upper edge along Γ-X_2 moves down. The dashed lines are transverse modes (deaf bands). In the marked frequency range, the displacement vectors (not shown here) are similar for the deaf mode propagating along the Γ-X_1 direction and the nondeaf mode propagating along the Γ-X_2 direction, but the wave vectors for both are perpendicular to each other.

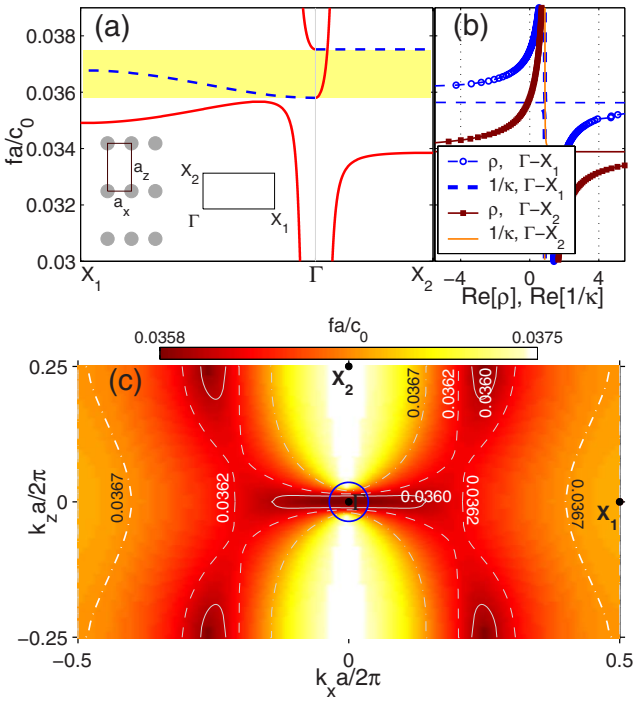

FIG. 2. (Color online) (a) Band structure for a rectangular lattice. The dashed lines represent deaf bands (transverse modes). Insets show the lattice ($a_x=a$, $a_z=2a$) and $\mathbf{k}=(k_x,k_z)$ directions in the first Brillouin zone. (b) Retrieved effective density ρ and the reciprocal of modulus $1/\kappa$ from reflection and transmission coefficients along Γ-X_1 and Γ-X_2 (real part). (c) Equal frequency contours (color shaded) in the first Brillouin zone for the frequency range marked in (a). The blue (dark gray) circle at the center is for the host at $fa/c_0=0.036$.

The effective mass density and bulk modulus of the metamaterial (relative to the host medium) near the resonant gap is shown in Fig. 2(b), retrieved by a procedure [34] from the reflection and transmission coefficients calculated by the layer multiple-scattering method. (For a plane wave incident normally on a slab of finite thickness, the refractive index $n=n_r+in_i$ and the impedance $\zeta=\zeta_r+i\zeta_i$ can be obtained from the reflection coefficient r and the transmission coefficient t. The effective density ρ and the reciprocal of effective modulus $1/\kappa$ are then directly calculated from $\rho=n\zeta$ and $1/\kappa=n/\zeta$.) In the frequency range of $0.035\,80<fa/c_0<0.037\,52$, the effective density along the Γ-X_1 (x) direction (ρ_x) is negative, and that along the Γ-X_2 (z) direction (ρ_z) is positive, while the effective modulus is nearly the same along these two orthogonal directions.

We plot in Fig. 2(c) the entire dispersion relation as a color-shaded contour plot for the frequency range marked in Fig. 2(a). In this marked frequency range ($0.035\,80<fa/c_0<0.037\,52$), the incoming wave at normal incidence cannot couple into the metamaterial (with its surface normal along the Γ-X_1 direction) because it encounters the deaf mode. From Fig. 2(c), we can see that part of the EFC (parallel to the Γ-X_1 direction, surface normal along Γ-X_2) for $fa/c_0=0.036$ is nearly flat. We can expect canali-

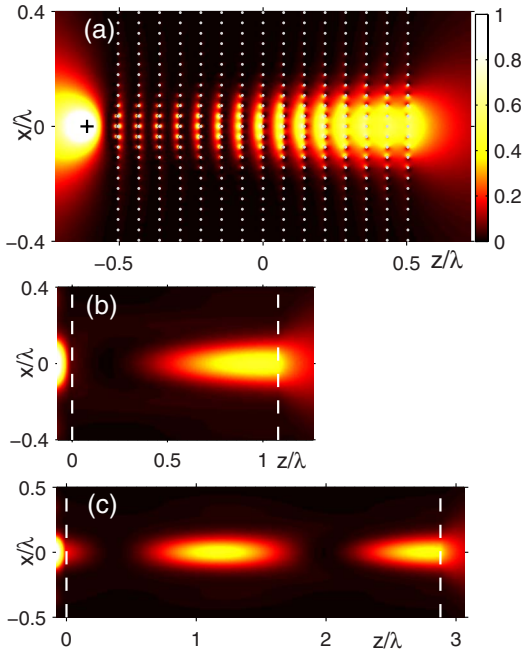

FIG. 3. (Color online) (a) Intensity of pressure field at $fa/c_0=a/\lambda=0.036$ for a slab geometry. The position of the line source is marked by "+." Gray dots denote the array of coaxially layered rods. (b), (c) Intensity of pressure field for a homogeneous slab with $\rho_x=-30$, $\rho_z=0.103$, and $1/\kappa=0.87$. The thickness of the slab is $30a$ in (b) and $80a$ in (c). The interfaces of the slab are marked by two dashed lines.

zation effect near this frequency. A slab of this metamaterial with surface normal along the elongated direction (Γ-X_2) can work as a transmission device which allows transportation of subwavelength images from one side to the other. The illustrative examples below are based on this result.

Figure 3(a) shows an example of transportation by a slab at $fa/c_0=0.036$. In the simulation, the slab has 51×15 ($x\times z$) rods with $a_x=a$ and $a_z=2a$. A line source is placed at a distance of $3a$ away from the first layer of the slab. The FWHM (full width at half maximum) of the beam at the exit surface is $\Delta=0.20\lambda$. *The width of the beam depends on the distance of the source away from the slab due to the contribution of evanescent waves.* To avoid the situation in which surface modes dominate the image [3], the thickness of the slab has been chosen such that the transmission coefficients for all propagating spatial harmonics are of the same order of magnitude. Figure 3(b) shows the situation for a homogeneous slab with thickness $30a$, and material parameters $\rho_x=-30$, $\rho_z=0.103$, and $1/\kappa=0.87$ as estimated from the retrieval procedure (Fig. 2). In both Figs. 3(a) and 3(b) we see that the intensity peak of the pattern inside the slab is near the exit surface. The profile of the pattern inside the slab actually depends on the thickness of the slab [see Fig. 3(c) for a homogeneous slab with thickness $80a$] due to the interference between waves reflected at the interfaces.

Figure 4(a) shows an example with a half cylindrical geometry which realizes the function of a far-field magnifying lens. The half cylindrical structure is a curved version of the rectangular array shown in Fig. 3(a). It has 11 layers along the radial direction. The radius of the first layer is $12.41a$,

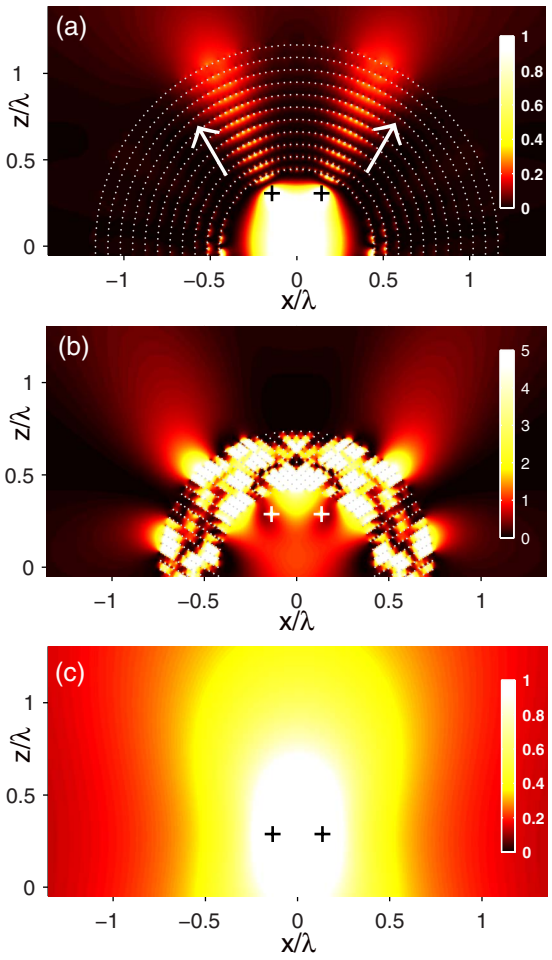

FIG. 4. (Color online) (a) Intensity of the pressure field for image transferring by a half cylindrical geometry using a rectangular lattice at $fa/c_0=a/\lambda=0.035\,93$. (b) The same as (a) but using a square lattice at $fa/c_0=0.0338$. (c) The propagating in free space at $fa/c_0=0.0338$. The positions of line sources (separated by $8a$) are marked by "+." The center of the cylindrical geometry is at the origin. Gray dots denote the array of coaxially layered rods.

and the radius of the successive layer is increased by $2a$. The distance between two neighboring sites along the circumference is a. The field from two lines sources (separated by $8a=0.287\lambda$) enters the composite and is guided to propagate along the radial direction. The collimated propagation along the radial direction magnifies the distance between the two point sources at the outer boundary. Once the separation between the two source points is magnified enough, subwavelength features can be imaged in the far field. For comparison, we plot in Fig. 4(b) the case corresponding to Fig. 1(b) [at $fa/c_0=0.0338$ (squarelike EFC) with the surface normal along the Γ-M direction], and in Fig. 4(c) the case without metamaterial. In Fig. 4(b), the half cylindrical structure has 14 layers along the radial direction; the radius of the first layer is $12.60a$; the radius of the successive layer is increased by $\sqrt{2}a/2$; and the distance between two neighboring sites along the circumference is $\sqrt{2}a$. From this figure, we cannot identify radial beams and the images, and the comparison demonstrates that the anisotropic EFC shown in Fig. 2(c) is important for far-field magnification. *The magnifying lens*

shown in Fig. 4(a) can naturally work in reverse to focus a beam.

In conclusion, we have designed a kind of two-dimensional acoustic metamaterial in which the effective densities are of opposite signs along two orthogonal directions. We demonstrated numerically that the highly anisotropic EFC of such metamaterial allows for the magnification of subwavelength features in the far field for acoustic waves. The working frequency can be tuned by changing the size and components of the coaxially layered rods. Such anisotropic resonance structures can do imaging for systems obeying scalar wave equations, and can be easily extended to vector waves.

This work was supported by HK-RGC through Grant No. 600305. Computation resources were supported by Shun Hing Education and Charity Fund. We thank W. Ren, Y. Lai, D. Z. Han, and Y. Jin for useful discussions.

[1] J. B. Pendry, Phys. Rev. Lett. **85**, 3966 (2000).
[2] V. G. Veselago, Sov. Phys. Usp. **10**, 509 (1968) [Usp. Fiz. Nauk **92**, 517 (1967)].
[3] C. Luo, S. G. Johnson, J. D. Joannopoulos, and J. B. Pendry, Phys. Rev. B **68**, 045115 (2003).
[4] P. A. Belov, C. R. Simovski, and P. Ikonen, Phys. Rev. B **71**, 193105 (2005).
[5] Y. Jin and S. He, Phys. Rev. B **75**, 195126 (2007).
[6] A. Salandrino and N. Engheta, Phys. Rev. B **74**, 075103 (2006).
[7] Z. Jacob, L. V. Alekseyev, and E. Narimanov, Opt. Express **14**, 8247 (2006).
[8] Z. Liu, H. Lee, Y. Xiong, C. Sun, and X. Zhang, Science **315**, 1686 (2007).
[9] I. I. Smolyaninov, Y. J. Hung, and C. C. Davis, Science **315**, 1699 (2007).
[10] I. V. Lindell, S. A. Tretyakov, K. I. Nikoskinen, and S. Ilvonen, Microwave Opt. Technol. Lett. **31**, 129 (2001).
[11] D. R. Smith and D. Schurig, Phys. Rev. Lett. **90**, 077405 (2003).
[12] S. A. Ramakrishna, J. B. Pendry, M. C. K. Wiltshire, and W. J. Stewart, J. Mod. Opt. **50**, 1419 (2003).
[13] D. Schurig and D. R. Smith, New J. Phys. **7**, 162 (2005).
[14] P. A. Belov and Y. Hao, Phys. Rev. B **73**, 113110 (2006).
[15] X. Li, S. He, and Y. Jin, Phys. Rev. B **75**, 045103 (2007).
[16] M. Ambati, N. Fang, C. Sun, and X. Zhang, Phys. Rev. B **75**, 195447 (2007).
[17] S. Yang, J. H. Page, Z. Liu, M. L. Cowan, C. T. Chan, and P. Sheng, Phys. Rev. Lett. **93**, 024301 (2004).
[18] X. Zhang and Z. Liu, Appl. Phys. Lett. **85**, 341 (2004).
[19] J. Li, Z. Liu, and C. Qiu, Phys. Rev. B **73**, 054302 (2006).
[20] Z. Liu, X. Zhang, Y. Mao, Y. Y. Zhu, Z. Yang, C. T. Chan, and P. Sheng, Science **289**, 1734 (2000).
[21] C. Goffaux, J. Sanchez-Dehesa, A. L. Yeyati, P. Lambin, A. Khelif, J. O. Vasseur, and B. Djafari-Rouhani, Phys. Rev. Lett. **88**, 225502 (2002).
[22] J. Li and C. T. Chan, Phys. Rev. E **70**, 055602(R) (2004).
[23] X. Hu, C. T. Chan, and J. Zi, Phys. Rev. E **71**, 055601(R) (2005).
[24] N. Fang, D. Xi, J. Xu, M. Ambati, W. Srituravanich, C. Sun, and X. Zhang, Nat. Mater. **5**, 452 (2006).
[25] Z. Liu, C. T. Chan, and P. Sheng, Phys. Rev. B **71**, 014103 (2005).
[26] J. Mei, Z. Liu, W. Wen, and P. Sheng, Phys. Rev. Lett. **96**, 024301 (2006).
[27] H. Larabi, Y. Pennec, B. Djafari-Rouhani, and J. O. Vasseur, Phys. Rev. E **75**, 066601 (2007).
[28] P. Lambin, A. Khelif, J. O. Vasseur, L. Dobrzynski, and B. Djafari-Rouhani, Phys. Rev. E **63**, 066605 (2001).
[29] N. A. Nicorovici, R. C. McPhedran, and L. C. Botten, Phys. Rev. E **52**, 1135 (1995).
[30] A. Moroz, Opt. Lett. **26**, 1119 (2001).
[31] M. Kafesaki and E. N. Economou, Phys. Rev. B **60**, 11993 (1999).
[32] Y. Lai, X. Zhang, and Z.-Q. Zhang, Appl. Phys. Lett. **79**, 3224 (2001).
[33] K. H. Fung, Z. Liu, and C. T. Chan, Z. Kristallogr. **220**, 871 (2005).
[34] D. R. Smith, S. Schultz, P. Markos, and C. M. Soukoulis, Phys. Rev. B **65**, 195104 (2002).